Old Dominion University Research Foundation

DEPARTMENT OF MECHANICAL ENGINEERING AND MECHANICS
COLLEGE OF ENGINEERING AND TECHNOLOGY
OLD DOMINION UNIVERSITY
NORFOLK, VIRGINIA 23529-0247

NAVIER-STOKES CALCULATIONS OF TRANSONIC FLOWS PAST CAVITIES

By

Oktay Baysal, Principal Investigator

Final Report
For the period January 16, 1988 to August 31, 1988

Prepared for the
National Aeronautics and Space Administration
Langley Research Center
Hampton, Virginia 23665

Under
Cooperative Agreement NCC1-121
Elizabeth B. Plentovich, Technical Monitor
TAD-NTF Operations Branch

September 1988

DEPARTMENT OF MECHANICAL ENGINEERING AND MECHANICS
COLLEGE OF ENGINEERING AND TECHNOLOGY
OLD DOMINION UNIVERSITY
NORFOLK, VIRGINIA 23529-0247

NAVIER-STOKES CALCULATIONS OF TRANSONIC FLOWS PAST CAVITIES

By

Oktay Baysal, Principal Investigator

Final Report
For the period January 16, 1988 to August 31, 1988

Prepared for the
National Aeronautics and Space Administration
Langley Research Center
Hampton, Virginia 23665

Under
Cooperative Agreement NCC1-121
Elizabeth B. Plentovich, Technical Monitor
TAD-NTF Operations Branch

Submitted by the
Old Dominion University Research Foundation
P. O. Box 6369
Norfolk, Virginia 23508

September 1988

ABSTRACT

This paper presents a computational investigation of subsonic and transonic flows past three-dimensional deep and transitional cavities. Computational simulations of these self induced oscillatory flows have been generated through time-accurate solutions of the Reynolds averaged full Navier-Stokes equations, using the explicit MacCormack scheme. The Reynolds stresses have been included through the Baldwin-Lomax algebraic turbulence model with certain modifications. Two cases have been computed to demonstrate the capability of the numerical scheme in modeling the complex three-dimensional flow features inside a cavity. The results from an experimental investigation have been used not only to benchmark the computations, but also to widen the database used for the discussions and conclusions. The computational results include instantaneous and time averaged flow properties everywhere in the computational zone. Time series analyses have been performed for the instantaneous pressure values on the cavity floor. The features of deep and transitional cavity flows, and the effect of the sidewall on the cavity flow flowfield are illustrated through computational graphics.

LIST OF SYMBOLS

c_p	pressure coefficient
D,L,W	depth, length, and width of the cavity, respectively
E	total energy
FF	front face
FP1,FP2	front and rear flat plates
J	jacobian of coordinate transformation
K	coefficient of thermal conductivity
M	Mach number

n	time index
p	static pressure
P_r	Prandtl number
R	universal gas constant
Re	Reynolds number
SFP	side flat plate
SW	side wall
T	static temperature
t	time
t	turbulent value index
t_c	characteristic time
RF	rear face
u,v,w	Cartesian velocity components
x,y,z	Cartesian coordinates
γ	ratio of specific heats
δ	boundary layer thickness
μ	viscosity coefficient
μ_t	eddy viscosity coefficient
ξ,η,ζ	generalized coordinates
ρ	density

INTRODUCTION

There are several types of researchers who study flows past cavities. Aerodynamicists are concerned with the drag due to a cavity, which may serve as a bay for weapons or special cameras, or a landing gear well on an aircraft (refs. 1, 2). Aeroacousticians study the sound waves generated by the self-induced oscillations of the flow inside a cavity, which can affect the

avionics and the people on board (refs. 3, 4). Fluid dynamicists are interested in the complex structure of the flow in a cavity (refs. 5-7). There exist both experimental (refs. 1-4) and computational (refs. 5-9) investigations on the flowfields of two and three dimensional rectangular cavities. Although work has been conducted from the subsonic to hypersonic regimes, most of the effort has been concentrated on the supersonic speed regime. In the subsonic and transonic regime, static pressure data have been sparse. Currently, there is no report that displays the complex transonic flow features inside the cavity. Also, because of renewed interest in high maneuverability and less radar detection signatures, which require internal carriage of weapons and stores, this research effort has been pursued.

As in the supersonic regime, there exist two distinct types of cavity flows when the approaching flow is transonic (refs. 1, 2). The first occurs when the cavity is deep, and it is called open cavity flow. In the case of an open cavity flow, the shear layer "bridges" the cavity opening. The other type of cavity flow is for shallow cavities, and it is termed closed cavity flow. In the case of closed cavity flow, the flow separates at the front face and reattaches on the cavity floor. The flow remains attached until it undergoes a separation due to high pressures ahead of the rear face. This creates two distinct separation regions, one downstream of the front face and another upstream of the rear face. Therefore the flow in a shallow cavity resembles that of the flow behind a rearward facing step followed by the flow ahead of a forward facing step. The parameter used to indicate the deepness or the shallowness of a cavity is its length-to-depth ratio, L/D (fig. 1).

There is a gradual change from closed to open cavity flow as the L/D ratio is decreased, which is called transitional cavity flow. Stallings and Wilcox (ref. 1) have found that transitional flow occurs for L/D's between 10

and 13 for supersonic freestream conditions. They also showed that there are hysteresis effects in the L/D region between 10 and 13 associated with the transitional flow in the supersonic regime. Although a similar study has not been conducted for the subsonic and transonic regimes, it is conceivable that the same trends exist in these flow regimes.

The results of the experimental investigation (ref. 2) used for comparison, has also been used to expand the database and knowledge of the flowfield in the cavities over the transonic regimes. These experiments have been conducted at the 7-by-10-Foot Transonic Tunnel of David Taylor Naval Ship Research and Development Center. The computations have been performed on the CYBER-205 (VPS-32) of NASA Langley Research Center.

GOVERNING EQUATIONS

The governing equations used in the computational analysis are the three-dimensional, time-dependent, compressible Navier-Stokes equations in terms of mass averaged variables. These equations can be written in Cartesian coordinates as follows:

$$(\partial Q/\partial t) + (\partial F/\partial x) + (\partial G/\partial y) + (\partial H/\partial z) = 0 \qquad (1)$$

$$Q = \begin{bmatrix} \rho \\ \rho u \\ \rho v \\ \rho w \\ \rho E \end{bmatrix} \quad F = \begin{bmatrix} \rho u \\ \rho uu - \tau_{xx} + p \\ \rho uv - \tau_{xy} \\ \rho uw - \tau_{xz} \\ \rho(E + p)u - k_1 \end{bmatrix} \quad G = \begin{bmatrix} \rho v \\ \rho uv - \tau_{xy} \\ \rho vv - \tau_{yy} + p \\ \rho vw - \tau_{yz} \\ \rho(E + p)v - k_2 \end{bmatrix}$$

$$H = \begin{bmatrix} \rho w \\ \rho uw - \tau_{xz} \\ \rho vw - \tau_{yz} \\ \rho ww - \tau_{zz} + p \\ \rho(E + p)w - k_3 \end{bmatrix} \tag{2}$$

The expressions for k_1, k_2, k_3, the shear stresses and heat fluxes can be written in tensoral shorthand notation as,

$$k_m = u_n \tau_{x_n x_m} - q_{x_m} \tag{3}$$

$$\tau_{x_n x_m} = \mu[(\partial u_m/\partial x_n) + (\partial u_n/\partial x_m) - 2/3(\partial u_\ell/\partial x_\ell)\delta_{mn}] \tag{4}$$

$$q_{x_m} = -K(\partial T/\partial x_m) \tag{5}$$

The perfect gas law,

$$p = (\gamma-1)[\rho E - \rho(u^2 + v^2 + w^2)/2] \tag{6}$$

and the Sutherland's laminar viscosity law have been used to complete the system of equations. δ denotes the Kronecker delta. For turbulent flow, the viscosity coefficient is defined as the sum of laminar viscosity (μ_l) and the turbulent eddy viscosity (μ_t). The governing equations (eqs. 1-6) have been transformed into generalized curvilinear coordinates in order to facilitate the stretched computational grids used in this study (fig. 2).

NUMERICAL PROCEDURE

The numerical scheme for the current problem is required to be time-accurate, highly vectorizable, and simple to code. The explicit MacCormack (ref. 10) scheme satisfies these conditions. This predictor-corrector explicit algorithm is summarized below in generalized coordinates.

Predictor Step:

$$\overline{Q^{n+1}} = Q^n - \Delta t\left[\Delta_\xi F^n + \Delta_\eta G^n + \Delta_\xi H^n\right] \tag{7}$$

Corrector Step:

$$Q^{n+1} = \frac{1}{2}\left(Q^n + \overline{Q^{n+1}}\right) - \frac{\Delta t}{2}\left[\nabla_\xi \overline{F^{n+1}} + \nabla_\xi \overline{G^{n+1}} + \nabla_\xi \overline{H^{n+1}}\right] \tag{8}$$

Δ denotes a forward spatial difference and ∇ denotes a backward spatial difference. This two step process (predictor-corrector) consists of evaluating derivatives by one-sided differences taken in opposite directions during alternate steps for symmetric calculations. As in any other centrally differenced scheme, fourth-order damping terms have been included explicitly. This scheme is second order accurate both spatially and temporally.

Cavity flows have been assumed symmetric with respect to the longitudinal center plane. Hence, the grids have been generated for a half-span cavity (figs. 1, 2). A two dimensional cartesian grid has been generated for the symmetry plane (x-y plane), with clustering of nodes near walls and in the shear layer region. This symmetry plane grid has been stacked in the z-direction, with clustering of these planes near the sidewall. The grid size of the L/D = 4.4 cavity is 111x71x28, and that of the L/D = 11.7 cavity is 121x71x28, in the longitudinal, normal, and lateral directions, respectively. Each grid has 15 nodes in the boundary layer at the front lip of the cavity. The computational zone is swept by the code plane-by-plane in the z-direction with vectorization done in each x-y plane. To ensure the longest possible data vectors neither with computational domain decomposition (ref. 9), nor with body fitted grids which would allow the mapping of the cavity surface to the ζ=0 plane (ref. 5), dummy points have been created for the regions under FP1, SFP, and FP2, from the y=0 plane to the y=D plane. Such a data vector

structuring and fully vectorizing the code has resulted in a processing rate of five microseconds per grid point per time step using 32-bit arithmetic on the CDC CYBER 205 of NASA Langley Research Center. This Fortran-200 code of the solution algorithm has been developed by Kumar (ref. 11).

Turbulence Model

The modeling of turbulence is complicated by the fact that several length scales exist which control the generation, transport, and dissipation of turbulent kinetic energy. Therefore, the standard two-layer algebraic turbulence model of Baldwin and Lomax (ref. 12) has been modified and used herein. It is based on the Boussinesq approximation of modeling the Reynolds stresses by an eddy viscosity, μ_t.

Modifications to the model have been done at all the points within the cavity as suggested in ref. 13. For these points,

$$\mu_t = \mu_{ts} + [\mu_{ts} - \mu_{tu}][1 - \exp\left(\frac{-\Delta x}{\lambda \delta}\right)] \tag{9}$$

Here μ_{ts} is the unaltered Baldwin-Lomax value, μ_{tu} is the computed eddy viscosity value at the upstream lip, and δ is the instantaneous boundary layer thickness at the upstream lip. Note that μ_{ts}, μ_{tu} and δ have been evaluated at the same spanwise location, and x is the streamwise distance from the upstream lip. λ is the relaxation length scale and has been chosen to be 10.

Modifications have been made to determine the proper length and velocity scales in regions of massive separation and three-dimensional corners. The first problem stemmed from the behavior of the velocity scale used in the wake function for the outer solutions, $F(n)$, which shows multiple peaks in the recirculation regions. In addition to a local peak in the attached boundary layer, a larger peak is caused by the overlaying vortex structure. The choice

of this second and larger peak as F_{max} would result in the outer (μ_t) value to be erroneously larger than if the first peak were picked. To eliminate this problem, the search for F_{max} has been cut off when the first peak was reached and the value of F(n) has dropped to 90% of this local maximum (ref. 14). The second problem has been the inclusion of multiple wall effects for points in the proximity of concave edges and corners. Eddy viscosity values have been computed using the vertical walls for such points, in addition to computing the eddy viscosity using the horizontal walls for all the points in the computation zone. Then an effective eddy viscosity has been computed as follows (ref. 15), for points near the corners

$$\mu_t = \left[\sum_{i=1}^{N_w} (\mu_t/y^+)_i\right]\left[\sum_{i=1}^{N_w} (y^+)_i^{-2}\right]^{-1/2} \qquad (10)$$

which increases the influence of the wall with the lowest y^+ value. N_w denotes the number of walls at a given corner. y^+ is constructed using the turbulent friction velocity, laminar viscosity and the normal distance to the wall.

Initial and Boundary Conditions

The entire flowfield above the cavity has been initialized with the inflow conditions. The flow velocities within the deep cavity are much lower than that of the freestream. Therefore, the velocity components inside the cavity have been arbitrarily specified as 10% of their free stream values. Since the shear layer impinges on the floor of the shallow cavity, an approximate velocity profile close to the inflow velocity profile has been specified within the cavity. The pressure and temperature within both cavities have been set to their free stream values.

No-slip boundary condition has been used on solid surfaces. These solid surfaces have been considered to be adiabatic. The pressures at the solid surfaces have been obtained from an extrapolation of the interior point values of pressure in the direction normal to the wall (i.e. zero normal gradient).

The values of u,v,w and T at the upstream boundary have been specified by a profile generated using the boundary layer equations. The pressure in this region, however, is extrapolated from the computation zone. This ensures the information to propagate upstream. The pressure inside the boundary layer has been maintained at the value extrapolated for the boundary layer edge. The flow variables at the downstream boundary, with the exception of pressure, have been obtained by zeroth-order extrapolation from the computation zone. The static pressure in this region has been specified to be at its freestream value. The outer boundary conditions have been specified by zeroth-order extrapolation for outflow, and as freestream conditions for inflow. The pressure values have always been assumed to be freestream value at this boundary since the normal flow has always been subsonic. The symmetry of the flow at the plane of symmetry (z=0) has been ensured by setting the z-component of velocity to zero and applying zeroth-order extrapolation for the other flow variables.

RESULTS AND DISCUSSION

The results of an experimental investigation have been used in this report for comparison purposes. The cavity flow model has been tested in the 7-by-10-Foot Transonic Wind Tunnel of David Taylor Naval Research and Development Center (ref. 2). A flat plate has been chosen as the parent body to simulate a generic aircraft configuration and to allow a well defined flow to develop ahead of the cavity. The cavity has been sized to be approximately

one-quarter scale, with a cavity length of 3.5 ft., a width of 0.8 ft., and a maximum depth of 0.8 ft. The floor of the cavity could also be moved to a cavity depth of 0.3 ft. The cavity L/D values tested have been 4.4 for the deep configuration (D=0.8 ft.) and 11.7 for the shallow configuration.

In order to establish a measure of time for this unsteady analysis, a characteristic time, t_c, has been loosely defined as the time it would take a fluid particle to travel the length of the cavity at freestream velocity.

Case 1: M = 0.9, Re/ft = 1.6×10^6, L/D = 4.4

The computer program has been run approximately 8.6 characteristic times (t_c). One t_c is 3.57 milliseconds (ms). The computational time for this case has been 15.5 CPU hours on the CYBER-205. The instantaneous velocity vectors at the plane of symmetry (Z/W = 0.0) are shown in fig. 3. As expected of deep cavities, the shear layer bridges the cavity opening. The organized behavior of the shear layer is evident. A large vortex encompasses the entire cavity. In addition to the main vortex structure, secondary vortices are visible near the corners. Shown in fig. 4 are the instantaneous streamlines within the cavity at three spanwise planes moving the plane of symmetry towards the sidewall (Z/W = 0.117, 0.294, 0.353). The direction of the flow is from right to left. As observed in the velocity vector plots, it is seen that the flow interacts with the rear face and forms a large vortex structure. As the sidewall is approached, the vortex structure changes its shape and size, and the core of the vortex moves towards the cavity opening. In addition to the main vortex structure, secondary vortices are seen at the corners. At Z/W = 0.353, a secondary separation is seen at the cavity floor close to the front face.

In order to depict the physics of mass expulsion and mass ingestion (which in turn causes the unsteady behavior), the density contours at two instants of time and at two spanwise planes have been displayed in fig. 5. At t_c = 7.20, the shear layer is deflected up, and mass is being expelled at the cavity rear face. The flow is compressed as it negotiates this deflection. There is a large region of separation on FP2 caused by the expansion at the sharp corner of the rear face. At the front face, the shear layer is deflected down into the cavity, causing the flow to expand. At t_c = 8.6, mass is being entrained into the cavity. Due to the deflection of the shear layer into the cavity at the rear face, the flow expands and then undergoes compression in this region. At the rear lip, the flow has to negotiate the 90° turn, thereby undergoing an expansion which is seen in the density contours. At the front face, the shear layer is parallel to the flat plate. Therefore the incoming flow does not undergo any expansion or compression. This clearly indicates the transient nature of the flow. Also, in the upstream lip region of the cavity, a sequence of compressions and expansions produced by the wavy structure of the shear layer can be observed.

Shown in fig. 6 are the instantaneous cross flow velocity vectors at two axial locations (X/L = 0.725, 0.978). Notice that the direction of flow is different at various axial locations (leaving or entering the cavity). Also, vortices are generated or dissipated at different cross sections.

The mean streamwise surface pressure coefficient distribution along the plane of symmetry are shown in fig. 7. The averaging has been started after running the program for 2 t_c, and it has been performed over 6 t_c thereafter. The experimental measurements have been averaged over one second. Good agreement between the computational and experimental (ref. 2) results has been obtained on the floor, the rear face, and the downstream flat plate (FP2).

The numerical results seem to be slightly overpredicting the pressure on the rear face towards the cavity floor. Spanwise C_p distributions on the rear face at 25%, and 62.5% depth are shown in fig. 7c, respectively. There is an increase in pressure towards the side wall, because the fluid is compressed as it reaches the rear face - sidewall intersection. Differences between the numerical solution and experimental data are notable on the rear face, where the magnitude of the fluctuating pressure is greatest and thus most sensitive to numerical inaccuracy. Also, the extent of separation has been slightly underpredicted on the aft section of the flat plate. The discrepancy between the computational and experimental results can be attributed to several reasons: (1) coarseness of the grids, (2) simplicity of the turbulence model, (3) explicit addition of artificial dissipation, (4) shorter period of averaging in the case of computations than that of measurements.

The instantaneous limiting streamline pattern on the cavity floor is shown in fig. 8a. The corresponding shear stress vectors on the cavity floor are shown in fig. 8b. The limiting streamlines qualitatively follow same trends as the skin friction lines. Close to the front face, the streamlines from opposite directions coverge on to a line of instantaneous separation. This separation causes the main vortex structure in the streamwise plane within the cavity. In addition to the main separation, a secondary closed type separation region is seen near the sidewall. Close to the rear face, the separated flow reattaches. Similar reattachment region is visible very close to the front face.

The frequency spectra at a point on the cavity floor is shown in fig. 9. It has been obtained by transforming the pressure histories from time domain into frequency domain (units in Hz) through fast Fourier transformations. Also, the pressure values have been converted from Pascals to decibels (dB) of

sound pressure levels (SPL). Since no experimental results are available for this case, a comparison is made with the Rossiter's prediction formula (ref. 3). The Rossiter's formula predicts the fundamental, second, and third harmonics to be f_1 = 78 Hz, f_2 = 183 Hz, and f_3 = 312 Hz, respectively. The fundamental and second harmonics computed herein agrees with the Rossiter's prediction within ±5Hz. The third harmonic has been smeared out, presumably due to numerical dissipation.

Case 2: M = 0.58, Re/ft = 1.52×10^6, L/D = 11.7

The computer program has been run approximately for 6 t_c. One t_c corresponds to 5.47 ms for this flow. The computational time for this run has been 15.0 CPU hours on the CYBER-205. Instantaneous velocity vectors in the streamwise plane at Z/W = 0.353 and at two instants of time (t_c = 5.2 and 6.0) are shown in fig. 10. For clarity, vectors are displayed at every alternate grid point in the streamwise direction. The shear layer in the front half of the cavity show a tendency to bridge the cavity opening. Halfway through the cavity opening, the shear layer deflects into the cavity towards the floor. The boundary layer on the floor grows from the point of reattachment towards the rear face. Due to the compression of the fluid near the rear face, the adverse pressure gradient causes the flow to separate and the shear layer deflects out of the cavity. Then the flow negotiates a 90° turn and separates on FP2. The velocity vectors show that in the front half of the cavity, the flow resembles an open cavity flow, and the rear half exhibits the trends of a closed cavity flow. This explains the reason for calling it a transitional cavity.

The instantaneous streamline plots at five spanwise locations are shown in figure 11. These plots show that the flow in the front half of the cavity

resembles that of a deep cavity flow and the shear layer impinges on the cavity floor. Beyond the point of impingement, the flow portrays the shallow cavity trends. The point of reattachment moves closer to the front face as the sidewall is approached. The presence of the sidewall influences the reattachment point due to the crossflow. In addition, the vortex structure changes from the plane of symmetry towards the sidewall. The instantaneous (t_c = 6) Mach contours at two spanwise planes (Z/W = 0.0, 0.47) are shown in figs. 12a and b. The shear layer is deflected out of the cavity at the rear face and the flow separates on FP2. The separation region shrinks in size as the side wall is approached. A representation of the crossflow structure is provided by fig. 13, where instantaneous (t_c = 6) cross flow velocity vector plots within the cavity are shown at two axial locations. The most prominent feature observed in these figures is the vortex structure which is caused by the cross flow mass ingestion from the lateral outboard at X/L = 0.55. This vortex structure moves from the cavity centerline towards the side wall at X/L = 0.98.

The mean wall pressure coefficients along the cavity centerline are shown in fig. 14. The averaging has been started after running the program for 2 t_c, and it has been performed over 4 t_c thereafter. The experimental measurements have been averaged over one second, which is approximately 183 t_c. The C_p distributions on the cavity front face, rear face, and the rear flat plate show good agreement with the experimental (ref. 2) data. Although, the C_p distribution on the cavity floor shows similar trends as observed experimentally, the reattachment point has been underpredicted by the computations. The discrepancies in the results could be attributed to the same reasons explained for the previous case.

The instantaneous limiting streamline pattern on the cavity floor is shown in fig. 15a. The corresponding shear stress vectors on the cavity floor are shown in fig. 15b. Close to the front face, the streamlines from opposite directions converge on to the separation line. In addition to the main separation, secondary closed separation can be observed. This separated flow reattaches on the cavity floor indicated by the reattachment line. From the point of reattachment, the flow remains attached to the floor until it reaches the rear face region. The separation pattern observed is rather complex. The flow separates in the streamwise and spanwise directions close to the sidewall. Within the main separation, a secondary horseshoe type separation structure is visible.

Shown in fig. 16 are the frequency spectra contributing to the overall sound pressure level at two positions along the cavity centerline. Both of the pressure pickup points have been located on the cavity floor. From experimental observations (ref. 4), it is known that there are no frequency modes which are excited for a closed cavity, and slightly more variations in the spectrum occur for a transitional cavity. This is attributed to the deflection of the shear layer attaching on the floor of the cavity, which partially prevents the feed- back mechanism from occuring. This feature is displayed in the computational predictions.

The discussions in the next subsections are based not only on the computational results of this report, but also on the results of references 2, 5-7.

Mach Number Effects

Cavity flows with various freestream Mach numbers have been compared at a Reynolds number range from 1.0×10^6 to 1.9×10^6 in the experimental

investigation of ref. 2. It has been observed that, in the case of deep cavities Mach number has only little effect on the cavity wall pressures over the Mach number range from 0.60 to 1.05. In comparison with the supersonic flow case for a deep cavity (ref. 6), it has been observed that, the values of C_p on the cavity floor towards the rear face and on the rear face decrease slightly from their values at low Mach numbers. It has also been observed that as the Mach number decreases in the subsonic and transonic regimes, a separation bubble exists on the flat plate downstream of the cavity (FP2).

The C_p distribution on the transitional cavity floor shows a plateau region, indicating the shear layer impingement on the floor in the lower Mach number (0.3 to 0.6) range. This trend is similar to the C_p distribution on the floor of a shallow cavity. As the Mach number increases, this plateau region slowly disappears and C_p distribution on the floor shows a monotonic increase. This is typical of a transitional cavity. The increase in Mach number affects the critical L/D ratio. Critical L/D refers to a particular ratio beyond which the flow behaves completely as a closed cavity flow, and below which it behaves as an open cavity flow. Therefore, the same trends as observed in the case of supersonic flows (refs. 1,5) are seen in the subsonic and transonic flow cases.

The parametric study of ref. 4 indicates that the sound pressure levels increase monotonically for deep and shallow cavities over a Mach number range of 0.6 to 1.0 for the first three frequency modes. However, for Mach numbers from 1.0 to 1.2, these levels either gradually drop or remain unchanged.

Effect of Boundary Layer Thickness

The effect of varying the ratio of the incoming boundary layer thickness to the cavity depth at the cavity lip is reported in ref. 1 for supersonic

flows. For a constant boundary layer thickness, when the cavity depth is increased (the ratio δ/D decreases), pressures on the rear face and aft region of the cavity floor also increase. This trend is observed in this computational study for subsonic and transonic flows. In the transonic flow case ($L/D = 4.4$ and $M = 0.9$), the ratio δ/D is 0.105, whereas in the supersonic flow case of refs. 5 and 6 ($L/D = 6.0$ and $M = 1.5$), this ratio is 0.25. Since the δ/D is smaller in the transonic deep cavity flow case, the pressure on the rear face and aft region of the floor is observed to be higher.

A comparison of C_p distribution on the cavity rear face for a transitional cavity ($L/D = 11.7$ and $M = 0.58$) and a shallow cavity from ref. 6 ($L/D = 16$ and $M = 1.5$) has also been made. The δ/D ratio of the shallow cavity case is 0.25 and that of the transitional case is 0.22. The same trend observed for deep cavities has been seen for the shallow and transitional cavities. That is, the C_p distribution on the rear face of the shallow cavity (larger δ/D) is slightly less than that of the transitional case (smaller δ/D).

CONCLUSIONS

Computational simulations of deep and transitional cavities at transonic regimes have been performed. The three-dimensional unsteady separation on the cavity floor has been analyzed, and computational flow visualization inside the cavity has been done. A parametric study, based on the current computational investigation as well as previous computational and experimental investigations has been conducted to investigate the effects of varying Mach number and the ratio δ/D. Both time averaged and instantaneous solutions have been obtained. Time averaged C_p has been compared with the experimental data of ref. 2. While most of this comparison is favorable, discrepancies in the

computational results occur on the floor and rear face of the cavity. These discrepancies can be attributed to several reasons; a) use of a simple turbulence model, b) averaging of the wall pressures have been done for a short period of time, in comparison with the experiments, c) explicit addition of artificial damping to smooth the numerical oscillations, and d) relatively coarser mesh than necessary for better turbulent calculations.

ACKNOWLEDGEMENT

This work has been supported under NASA Grant No. NCC-1-121.

REFERENCES

1. Stallings, R. L. and Wilcox, F. J., "Experimental Cavity Pressure Distributions at Supersonic Speeds," NASA-TP-2683, June 1987.

2. Plentovich, E. B., "Study of Three-Dimensional Cavity Flow At Transonic Speeds," AIAA Paper 88-2032, May, 1988.

3. Rossiter, J. E., "Wind Tunnel Experiments on the Flow Over Rectangular Cavities at Subsonic and Transonic Speeds," RAE-ARC-R&M 3438, 1966.

4. Shaw, L. L., "Supersonic Flow Induced Cavity Acoustics," 56th Shock and Vibration Symposium, Monterey, CA, October 1985.

5. Baysal, O. and Stallings, R. L., Jr., "Computational and Experimental Investigations of Cavity Flowfields," AIAA Journal, Vol. 26, No. 1, January 1988.

6. Baysal, O., Srinivasan, S. and Stallings, R. L., Jr., "Unsteady Viscous Calculations of Supersonic Flows Past Deep and Shallow Three-Dimensional Cavities," AIAA Paper 88-0101, January 1988.

7. Srinivasan, S., "Numerical Simulation of Turbulent Three-Dimensional Cavity Flows," Ph.D Dissertation, Old Dominion University, Norfolk, Virginia, August 1988.

8. Rizzeta, D. P., "Numerical Simulation of Supersonic Flow Over a Three-Dimensional Cavity," AIAA Paper 87-1288, June 1987.

9. Suhs, N. E., "Computations of Three-Dimensional Cavity Flow at Subsonic and Supersonic Mach Numbers," AIAA Paper 87-1208, June 1987.

10. MacCormack, R. W., "The Effect of Viscosity in Hypervelocity Impact Cratering," AIAA Paper 69-354, April 1969.

11. Kumar, A., "Numerical Simulation of Flow Through Scramjet Inlet Flowfield Using the 3-D Navier-Stokes Code," AIAA Paper 85-1664, July 1985.

12. Baldwin, B. S. and Lomax, H., "Thin-Layer Approximation and Algebraic Model for Separated Turbulent Flows," AIAA Paper 78-257, January 1978.

13. Waskiewicz, J. D., Shang, J. S. and Hankey, W. L., "Numerical Simulation of Near Wakes Utilizing a Relaxation Turbulence Model," AIAA Journal, Vol. 18, No. 12, December 1980, pp. 1440-1445.

14. Degani, D. and Schiff, L. B., "Computation of Supersonic Viscous Flows Around Pointed Bodies at Large Incidence," AIAA Paper 83-0034, January 1983.

15. Gorski, J., Ota, D. K. and Chakravarthy, S. R., "Calculation of Three Dimensional Cavity Flow Fields," AIAA Paper No. 87-0117, January 1987.

FIGURES

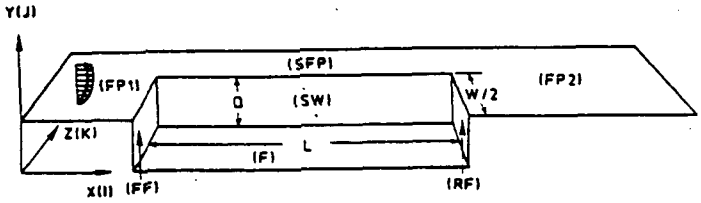

Fig. 1 Schematic of a rectangular half-span cavity

Fig. 2 Three-dimensional grid structure for a half-span rectangular cavity.

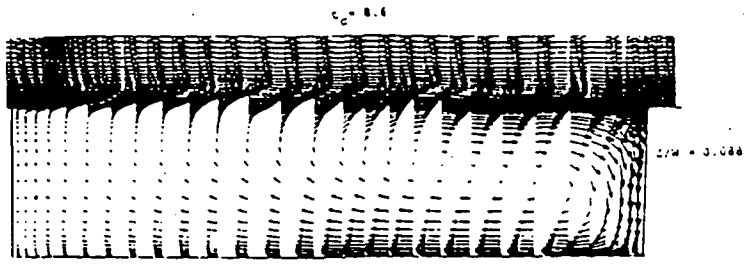

Fig. 3 Instantaneous streamwise velocity vectors of Case 1.

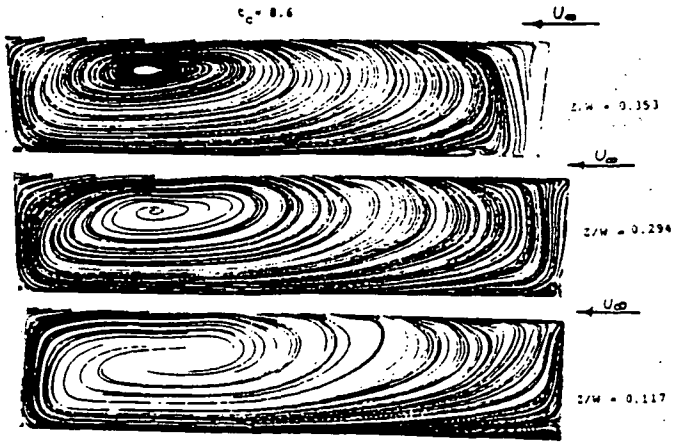

Fig. 4 Instantaneous streamlines of Case 1, at three spanwise planes.

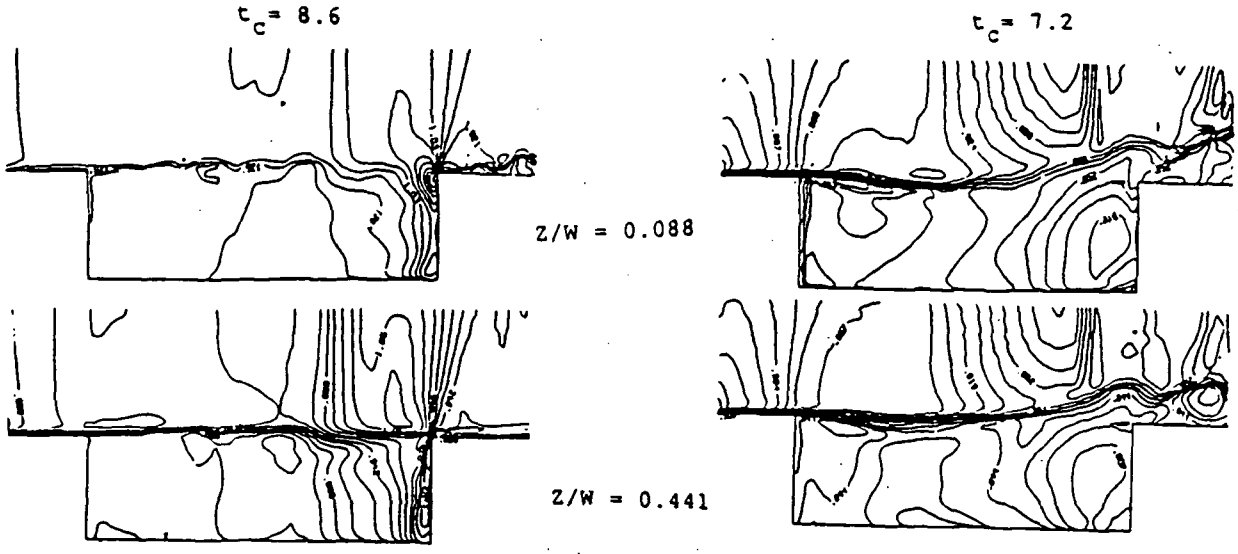

Fig. 5 Instantaneous density contours of Case 1, at two spanwise planes and two time instants.

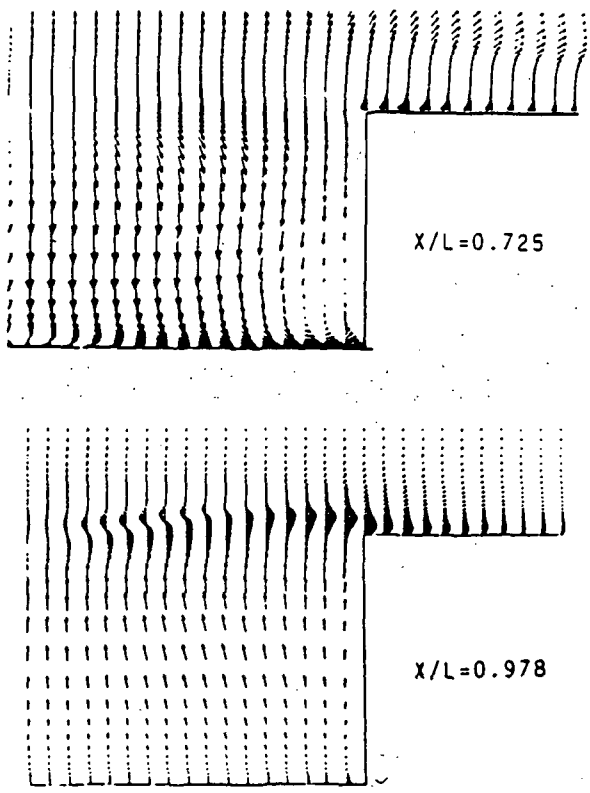

Fig. 6 Instantaneous (t_c=8.6) cross flow velocity vectors at two axial locations. (Case 1) (X/L = 0.725, 0.978)

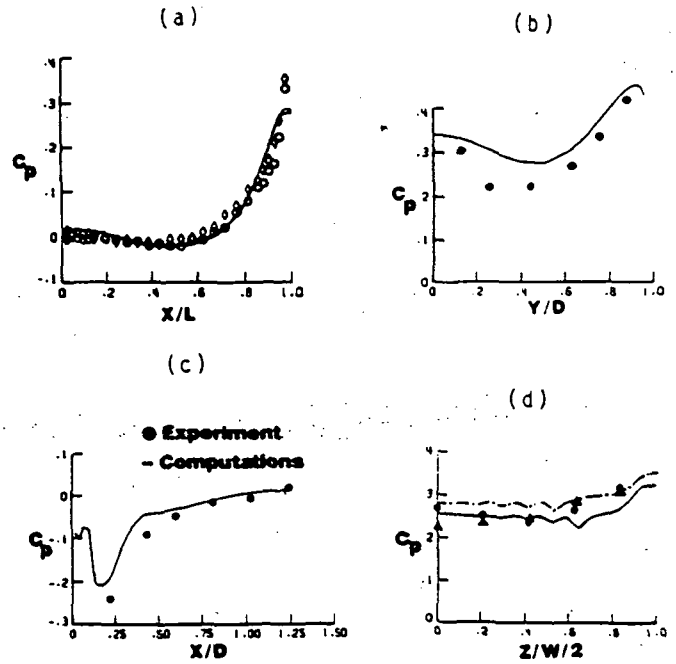

Fig. 7 Mean surface pressure coeff. distribution of Case 1. (a) along the floor at Z/W=0.0 (— CFD, o Exp), and at Z/W=0. (-- CFD, ◇ Exp), (b) along the centerline of RF (—CFD. • EXP (c) along the centerline of FP (d)spanwise variation on RF at Y/D=0.25 (---CFD, • Exp) and at Y/D=0.625 (-•- CFD, ▲Exp).

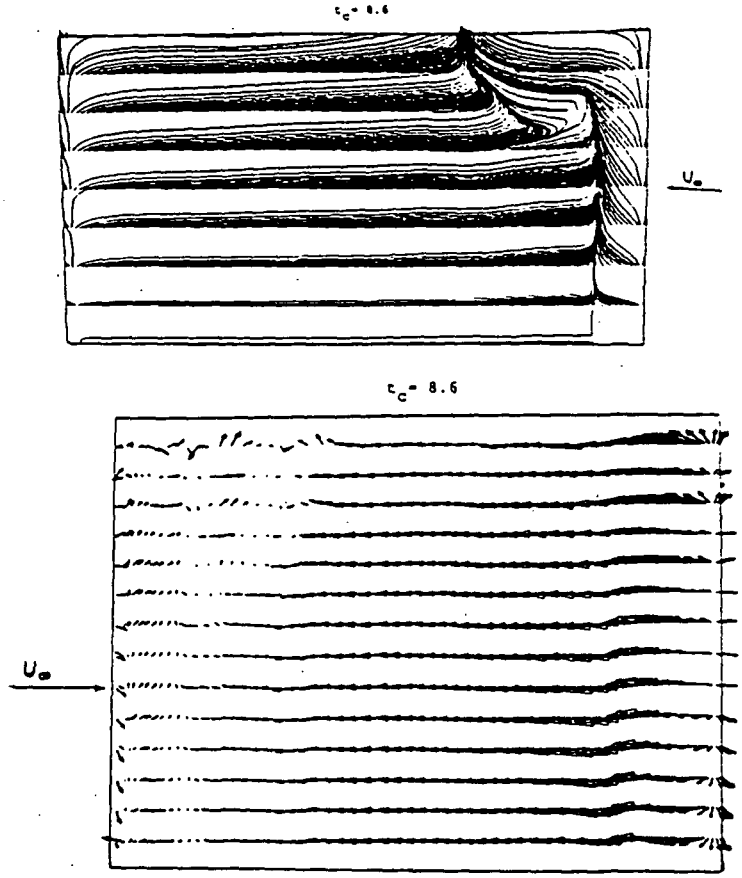

Fig. 8 Instantaneous (a)limiting streamlines (b) shear stress vectors, of case 1, on the cavity floor.

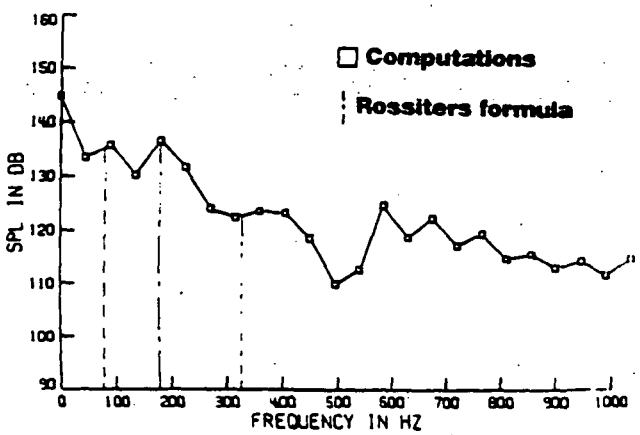

Fig. 9 Frequency spectra of sound pressure levels (SPL) on the cavity floor at X/L = 0.30. (Case 1)

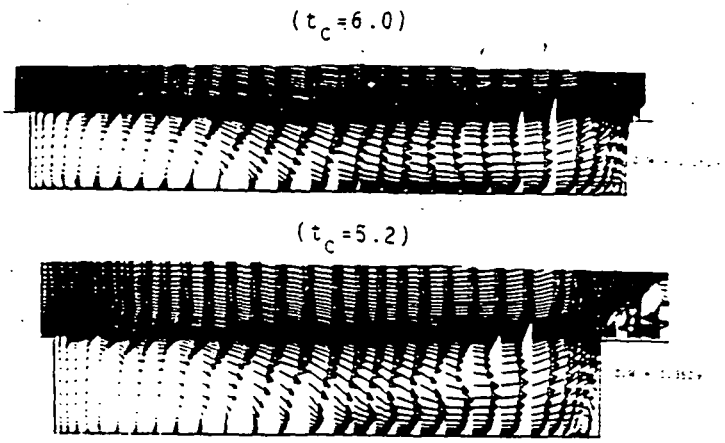

Fig. 10 Streamwise distribution of velocity vectors at two time instants, (t_c=5.2,6.0), Case 2

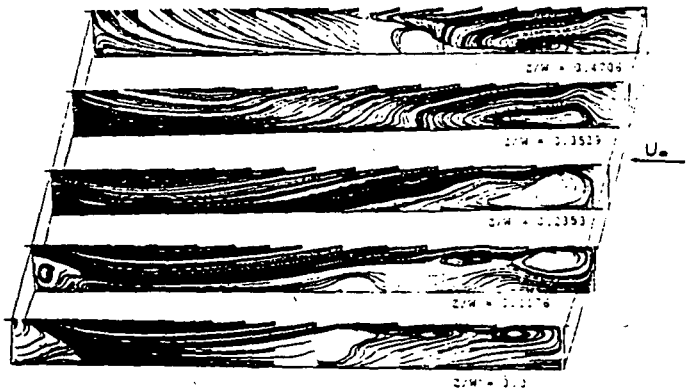

Fig. 11 Instantaneous streamlines at at five spanwise planes for Case 2.

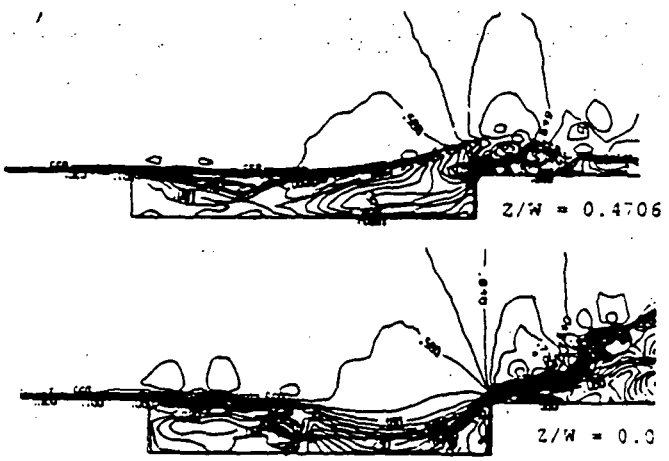

Fig. 12 Instantaneous Mach number contours at two spanwise planes for Case 2.

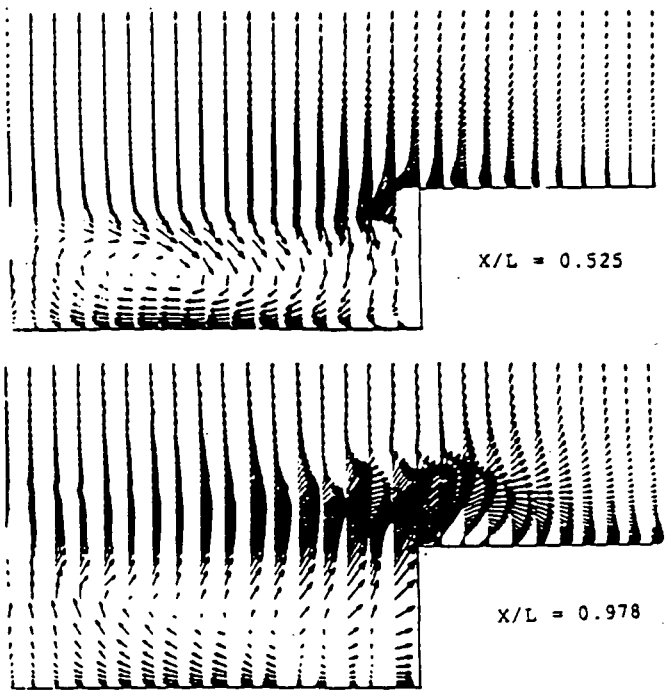

Fig. 13 Instantaneous (t_c = 6) cross flow velocity vectors at two axial planes. (Case 2)

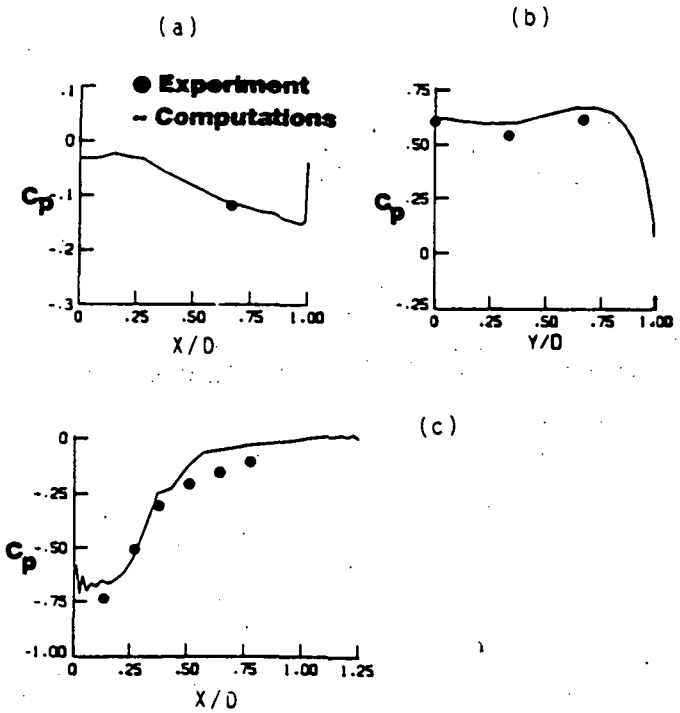

Fig. 14 Mean surface pressure coeff. distribution of Case 2, along the centerline of (a) FF, (b) RF, (c) FP2, (d) floor, (e) spanwise variation on th rear face at Y/D=0.5.

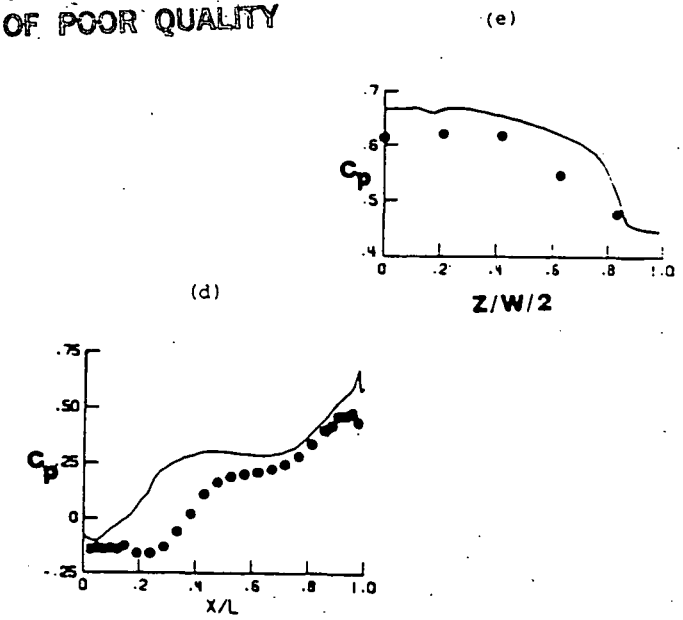

Fig. 14 Concluded.

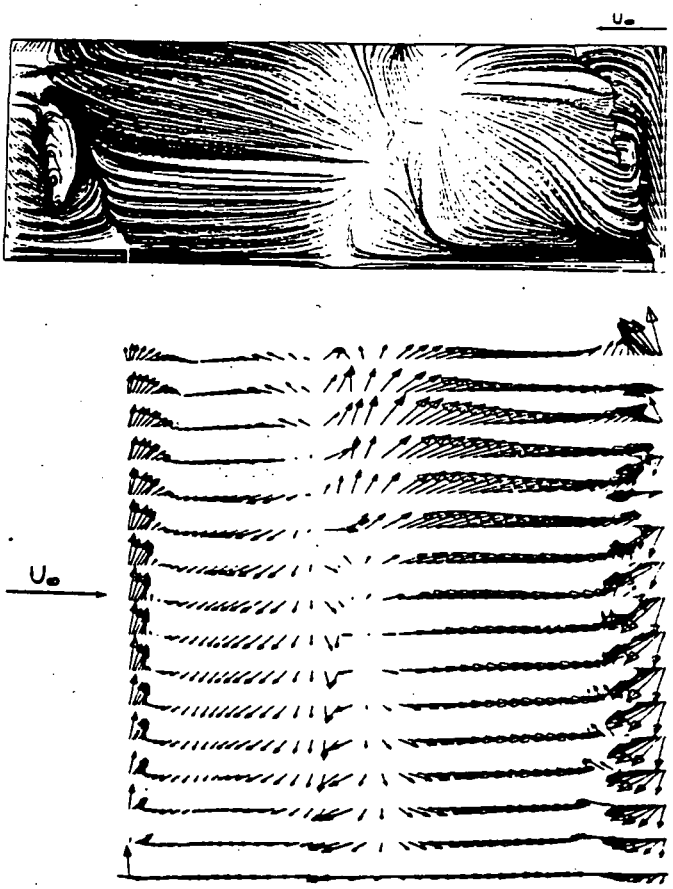

Fig. 15 Instantaneous (a) limiting streamlines, (b) shear stress vectors on the cavity floor. (Case 2)

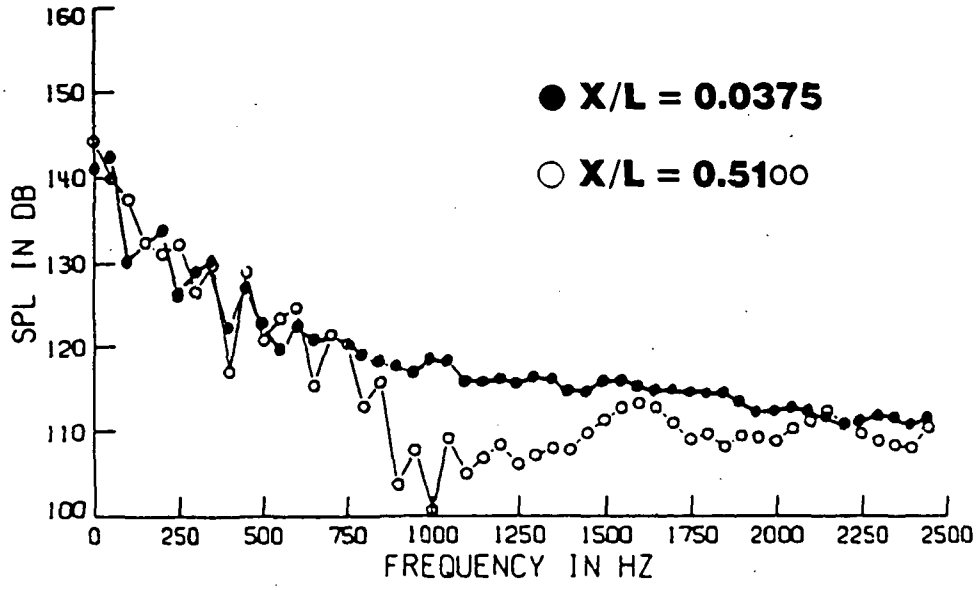

Fig. 16 Frequency spectra of sound pressure levels (SPL) on the cavity floor at two axial locations. (Case 2)